actuators

MDPI

Article

Design and Applications of High Force Generation in 3D-Printed Pneumatic Artificial Muscles

Jae Hyeong Park, Seungweon Jeon, Young Jin Gong, Jimin Yoon, Dongsu Shin, Hyeon-Woong Seo, Bo Geun Kim, Ja Choon Koo, Hyungpil Moon, Rodrigue Hugo and Hyouk Ryeol Choi *

School of Mechanical Engineering, Sungkyunkwan University, 2066, Seobu-ro, Jangan-gu, Suwon-si 16419, Gyeonggi-do, Republic of Korea; csp00275@skku.edu (J.H.P.); jeon4567@g.skku.edu (S.J.); youngjin510@skku.edu (Y.J.G.); lepenseur@g.skku.edu (J.Y.); anaud94@g.skku.edu (D.S.); hwseo0103@g.skku.edu (H.-W.S.); thana@g.skku.edu (B.G.K.); jckoo@skku.edu (J.C.K.); hyungpil@g.skku.edu (H.M.); rodrigue@skku.edu (R.H.)

* Correspondence: choihyoukryeol@gmail.com

Abstract: Increasing the force generation and scalability of soft pneumatic actuators poses significant challenges in robotics applications, especially where high load capacities and precise control are required. This paper presents UniBPAM, a novel, scalable soft pneumatic actuator optimized through 3D printing to enhance force generation. By analyzing design parameters, such as the number of sides, height, and origami factor, UniBPAM achieved a 21.48% increase in force generation. Scalable across diameters from 36 to 144 mm, the actuator demonstrated the ability to lift up to 57 kg with 84.9% strain at larger scales. Additionally, the BiBPAM variant enables bidirectional actuation in robotic joints via motion control, which is realized through PID systems, making it suitable for various robotic applications.

Keywords: soft actuators; pneumatic artificial muscles; 3D-printed; soft robotics

check for updates

Citation: Park, J.H.; Jeon, S.; Gong, Y.J.; Yoon, J.; Shin, D.; Seo, H.-W.; Kim, B.G.; Koo, J.C.; Moon, H.; Hugo, R.; et al. Design and Applications of High Force Generation in 3D-Printed Pneumatic Artificial Muscles. *Actuators* **2024**, *13*, 436. https://doi.org/10.3390/act13110436

Academic Editor: Alessio Merola

Received: 8 October 2024
Revised: 27 October 2024
Accepted: 29 October 2024
Published: 30 October 2024

Copyright: © 2024 by the authors. Licensee MDPI, Basel, Switzerland. This article is an open access article distributed under the terms and conditions of the Creative Commons Attribution (CC BY) license (https://creativecommons.org/licenses/by/4.0/).

1. Introduction

Robotic actuators are fundamental components that determine the motion capabilities and applications of robots. Traditional actuators, such as electric motors and hydraulic systems, provide substantial force. However, they are often heavy and rigid, and they lack compliance, limiting their use in applications requiring safety and adaptability. These limitations have driven interest in soft actuators, which are lightweight, flexible, and capable of safe interactions with humans and unstructured environments [1–3].

One of the earliest soft actuators developed is the McKibben muscle, known for its ability to generate large forces through the pneumatic inflation of a braided mesh surrounding an inner rubber tube [4–6]. Although McKibben muscles can produce significant force, they typically realize only approximately 30% strain and are limited to unidirectional contractions.

To achieve higher strain, expansion-type soft pneumatic actuators, which operate under positive pressure to generate motion, have been introduced [7–9]. These actuators offer greater strain capabilities but often require intricate manufacturing techniques, resulting in reduced force generation and complex fabrication processes.

Alternatively, contraction-type soft pneumatic actuators operating under negative pressure have been developed to achieve high strain during contraction [10–13]. A notable example is the fluid-driven origami-inspired artificial muscle (FoAM), which uses foldable structures to enable large deformations under vacuum pressure. Specifically, FoAM achieves high strains (>90%) and generates a moderate force capable of supporting a payload of up to 22 kg, making it effective in applications requiring large contractions.

To address the need for both high force generation and high strain under negative pressure, actuators with significantly increased contraction ratios using vacuum have been developed [14–16]. Among these, the origami-based vacuum pneumatic artificial muscle

(OVPAM) is notable for its superior performance. OVPAM utilizes an origami-inspired design to achieve large contraction ratios (~87%) and substantial force generation, capable of lifting loads up to 40 kg [14]. By preventing lateral contraction of the film during actuation, the discrete plates enable both high force generation and large contraction ratios.

Although both positive and negative pressures can result in high contraction ratios, achieving active bidirectional actuation remains challenging. To overcome this, researchers have developed actuators capable of bidirectional actuation using both positive and negative pressure [17–19]. Notably, the bidirectional pneumatic artificial muscle (BiPAM) [19] achieves bidirectional motion, with a strain of 402% during expansion and 75% during contraction, while supporting a payload of up to 12 kg in both directions. However, its overall performance in terms of force and strain remains moderate.

Despite these advancements, the complexity and fabrication difficulties associated with these actuators remain unresolved. To address these challenges, researchers have explored three-dimensional (3D) printing techniques for actuator development [20–26]. Linear soft vacuum actuators (LSOVA) and various 3D-printed actuators have been introduced [23]. Although LSOVA offers moderate strain and ease of fabrication through 3D printing, it often compromises force generation owing to inherent limitations in the 3D printing process. Specifically, the overhang issue restricts the fabrication of wide geometries in a single-material print, limiting the ability of the actuator to generate higher forces (~27 N). Additionally, LSOVA is typically limited to unidirectional actuation.

In this study, recognizing the need for actuators that combine high force, high strain, bidirectional operation, and ease of fabrication, we propose a novel soft pneumatic actuator that overcomes the limitations of existing designs. This actuator offers several key advantages.

- Performance enhancement: Key design parameters, such as the number of sides, height, and origami factor, have been analyzed and optimized, leading to significant improvements in force generation. This optimization results in an approximately 21% increase in force compared to the initial design.
- Easy fabrication via 3D printing: Traditional origami-based actuators often require cutting and folding 2D patterns to create the lateral structure, which limits design flexibility. Conversely, our actuator utilizes 3D printing technology to fabricate complex three-dimensional structures directly. This approach simplifies the fabrication process, enables rapid prototyping, and facilitates the efficient testing of various geometric configurations.
- Scalability: The actuator exhibits consistent performance across a range of diameters, from 36 mm to 144 mm. This scalability allows for customization based on the required force output. Users can adjust the actuator size to accommodate delicate tasks with smaller actuators or increase force generation for larger-scale applications.
- Bidirectional force transmission: This actuator is capable of transmitting force in both directions, enabling torque generation in robotic rotary joints. This bidirectional capability allows the actuator to perform tasks such as rotating or reversing motion under load without the need for additional actuators, thereby enhancing system efficiency and reducing complexity.
- Applications: The actuator, along with its control system, has been applied to robotic joints for the position control of a forearm and an upper arm. Tendons connected to pulleys transmit force for controlled rotation, and the system's position control has been evaluated to verify its functionality in robotic movement.

By addressing the limitations of existing actuators, such as fabrication complexity, unidirectional actuation, and limited scalability, our proposed design has the potential to significantly expand applications in the field of soft robotics, where high performance and adaptability are crucial (Table 1).

Table 1. Comparison of the performance characteristics of various pneumatic actuators.

	McKibben Muscle	FoAM	OVPAM	BiPAM	LSOVA	This Work
Force	●	◗	●	◗	❍	●
Strain	❍	●	●	●	◗	●
Ease of Fabrication	❍	●	❍	❍	●	◗
Pressure	P	N	N	P/N	N	P/N
Scalability	O	O	O	X	O	O
Bidirectional Actuation	X	X	X	O	X	O

Note: ● = high, ◗ = moderate, ❍ = low, P = positive pressure, N = negative pressure,O = yes, and X = no.

This paper is organized as follows. Section 2 explains the design of the unidirectional actuator, detailing its working principle, fabrication process, and performance improvements via experimental validation. In Section 3, we extend the discussion by introducing a bidirectional actuator and describing its application in robotic joints. This section outlines the control system architecture and mechanical integration, followed by a detailed description of its implementation in the forearm and upper arm joints, demonstrating the actuator's capability for bidirectional torque and precise joint movement control.

2. Actuator Design

2.1. Configuration and Operating Principle

The configuration of the proposed actuator is shown in Figure 1a. The actuator comprises a flexible lateral pattern and rigid components. The lateral pattern is 3D-printed using TPU (SainSmart, 95A, Black, USA) with a Prusa MK3+ printer (Prusa Research, Holešovice, Czech Republic), while the rigid parts, including the top cap, bottom cap, and radial constraint, are 3D-printed using PLA (eSun PLA+ White) with a Bambu Lab P1S printer (Bambu Lab USA Inc., Austin, TX, USA). Following 3D printing, the rigid and flexible components are bonded with adhesive (Loctite 401, Loctite, Newington, CT, USA) to ensure a strong, durable connection and prevent air leakage (Figure 1b).

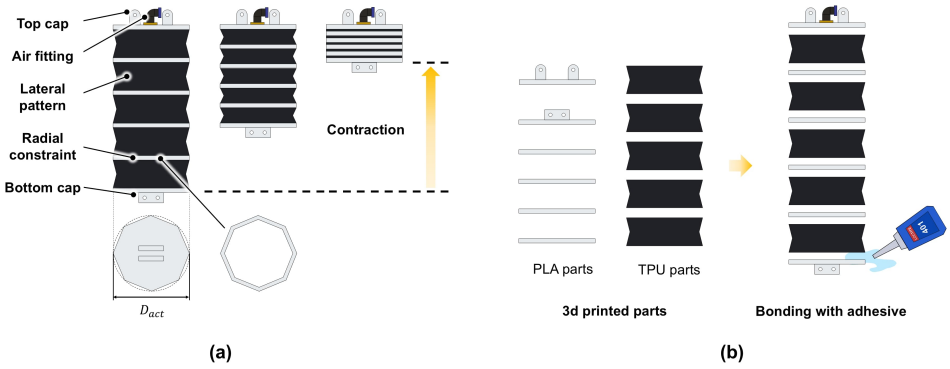


Figure 1. (**a**) Actuator configuration and its operating principle. (**b**) Fabrication process of the actuator.

The actuator is designed to deform under pressure, allowing axial contraction and expansion while maintaining constant circumferential dimensions. The top cap includes a pneumatic fitting for internal pressure adjustment via an air tube. By modulating the internal pressure, the actuator generates a contractile force.

The work and force produced via the actuator system are described as follows:

$$W_{act} = W_{air} - U_{elastic} \tag{1}$$

Differentiating Equation (1) with respect to x, we obtain Equation (2):

$$\frac{dW_{act}}{dx} = \frac{dW_{air}}{dx} - \frac{dU_{elastic}}{dx} \tag{2}$$

Given that the work performed per unit distance is equivalent to the force, it can be expressed as follows:

$$F_{act} = F_{air} - F_{elastic} \tag{3}$$

Here, F_{air} can be expressed as

$$F_{air} = P\frac{dV}{dx} \tag{4}$$

where P denotes the internal pressure, and $\frac{dV}{dx}$ denotes the rate of change in volume with respect to displacement. Substituting F_{act} into $F_{act} = F_{air} - F_{elastic}$ allows the forces generated under different pressure conditions to be predicted.

In these equations, W_{act} denotes the work performed via the actuator, defined as the difference between the work done via the internal air pressure (W_{air}) and the elastic potential energy stored in the actuator's flexible sections ($U_{elastic}$). Similarly, F_{act} denotes the force exerted via the actuator, which is the difference between the force exerted via air pressure (F_{air}) and the elastic force resisting the actuator's deformation ($F_{elastic}$).

Given the hyperelastic properties of TPU and the complexity of the origami-inspired structure, it is challenging to analytically derive F_{elastic}. Although finite element method (FEM) simulations could be employed for this purpose, they are computationally intensive and time-consuming. To address this, we opted to bypass simulations and directly measure F_{act} experimentally. This approach allows for a more accurate and efficient analysis of actuator performance, avoiding the need for complex computational methods.

2.2. Actuator Test

The lateral pattern of the actuator is determined by the design variables n, D, h, p, o, θ, and t, as illustrated in Figure 2a. The definitions of these parameters are as follows:

- n: number of sides of the polygon.
- D: diameter of the circumscribed circle of the polygon, set arbitrarily to 72 mm, similar to the diameter of a human forearm.
- h: height of a single pattern unit.
- p: parameter ranging from 3 to 10 that determines the size and shape of the parallelepiped cuts removed from the lateral surface of the n-prism, shaping the lateral pattern.
- o: origami factor, a normalized version of p that controls the degree of the origami pattern, defined as

$$o = \frac{p - p_{\min}}{p_{\max} - p_{\min}} \tag{5}$$

  When $o = 0$ (i.e., $p = 3$), there is no origami pattern, resulting in a straight, bellows-like structure. Conversely, $o = 1$ (i.e., $p = 10$) indicates the maximum presence of the origami pattern.
- θ: angle between the ground and pattern, set to the minimum slope angle that the 3D printer can produce, ensuring manufacturability.
- t: thickness of the lateral pattern, set to 0.5 mm, as experiments have shown that no air leakage occurs at this thickness.

The lateral pattern is created by forming an n-sided prism, removing parallelepiped shapes from its lateral surface based on the parameter p, and then applying a circular pattern using the shell function. By adjusting p and, consequently o, we can effectively control the degree of the origami pattern in the design of the actuator.

Therefore, once the design variables n, h, and o (derived from p) are determined, the shape of the lateral pattern is determined. The goal of this study is to design an actuator with the maximum payload capacity by maximizing the force generated at full contraction. However, owing to experimental limitations, we could not accurately measure the force at a 100% contraction level (full contraction) because the load cell, which operates based on strain measurements, was unable to detect the force without further deformation in the fully contracted state.

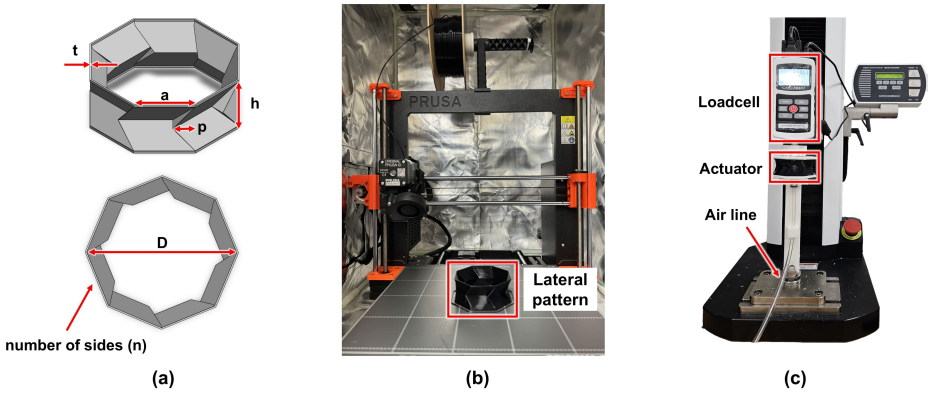


Figure 2. (**a**) Design parameters of the actuator, including n, D, h, p, θ, and t. (**b**) 3D-printed lateral pattern fabricated using a Prusa MK3+ printer. (**c**) Tensile testing setup.

To address this issue, we performed an optimization based on the force measured at the 80% contraction level. This approach allowed us to approximate the maximum payload capacity as the force decreased from 0% to 100% contraction levels. Figure 3b illustrates this trend, showing that the force output of the actuator decreases as the contraction level increases. By focusing on an 80% contraction level, reliable data can be obtained while capturing the behavior near full contraction.

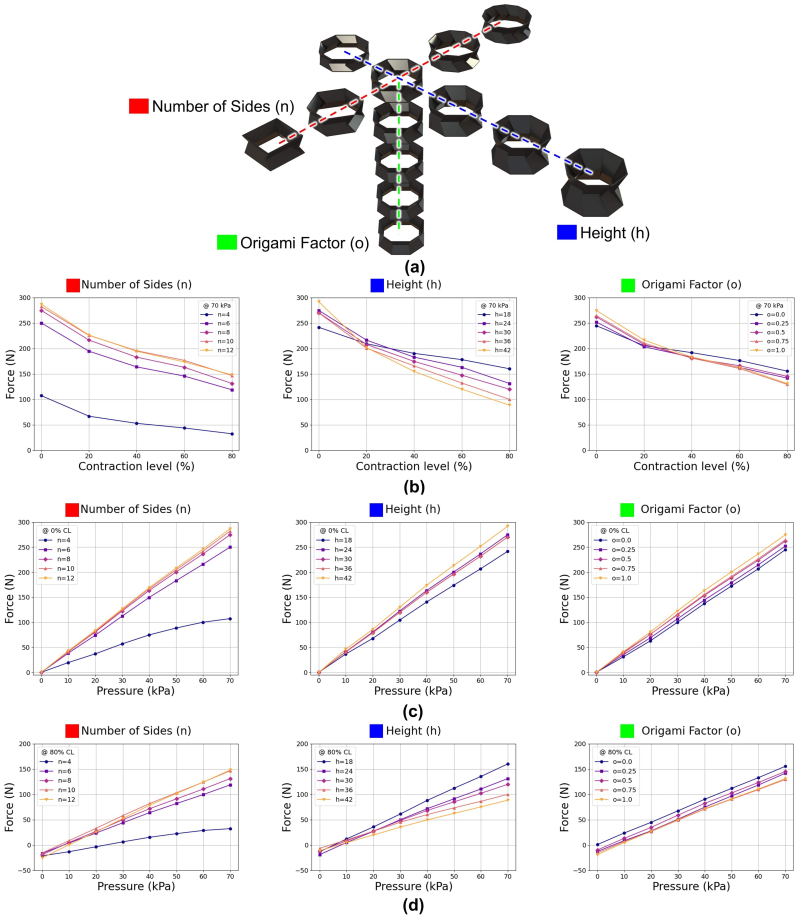


Figure 3. (**a**) Parametric variation of the experimental models: number of sides n in red, height h in blue, and origami factor o in green. (**b**) Force vs. contraction level graphs at 70 kPa pressure for different parameters. (**c**) Force vs. pressure graphs at 0% contraction level for various parameters. (**d**) Force vs. pressure graphs at 80% contraction level for various parameters.

The objective function is defined as the force $F_{act}(n, h, o)$ generated via the actuator at a specific contraction level and pressure. This optimization is crucial for ensuring that the actuator can effectively handle the required payload.

This study adopted an approach inspired by multi-criteria decision making (MCDM), in which each design parameter—namely n, h, and o—was evaluated for its influence on force generation. The optimal configuration was determined by synthesizing the best values for each parameter to achieve the highest performance in pneumatic actuators [27,28].

The patterns determined by the design variables n, h, and o are 3D-printed, as shown in Figure 2b. Each actuator, composed of a single layer, is attached to a tensile testing machine to conduct experiments, as shown in Figure 2c.

The experiments were conducted by measuring the force while varying the pressure at different contraction levels, expressed as a percentage of the maximum contraction of the actuator. Specifically, the maximum possible contraction of the actuator was defined as 100%, with measurements taken at contraction levels of 0% (no contraction), 20%, 40%, 60%, and 80% of the maximum contraction. At each contraction level, the pressure was varied from 0 kPa to 70 kPa in 10 kPa increments while the force was measured.

Therefore, the performance of the actuator was analyzed and optimized under quasistatic conditions using data from the 80% contraction level. The standard model is arbitrarily defined as $(n, h, o) = (8, 24, 1)$. Based on this model, the values of the design variables were expanded and set as follows:

$$\text{Maximize} \quad F_{act}(n, h, o) \quad \text{at 80\% contraction level and 70 kPa pressure}$$

Subject to:

$$\begin{aligned} n &\in \{4, 6, 8, 10, 12\}, \\ h &\in \{18, 24, 32, 40, 48\}, \\ o &\in \{0, 0.25, 0.5, 0.75, 1\}. \end{aligned}$$

The effects of the design parameters—the number of sides n, height h, and origami factor o—on the force generated via the actuator are investigated under various contraction levels and pressure conditions, as illustrated in Figure 3. The design space depicted in Figure 3a visually demonstrates how the lateral pattern changes with different values of n, h, and o. In this visualization, n varies along the red axis, h varies along the blue axis, and o varies along the green axis, clearly highlighting the structural variations corresponding to these parameters.

At a constant pressure of 70 kPa, the force decreases as the contraction level increases (Figure 3b). This behavior aligns with the general characteristics of the actuator, indicating that the maximum payload capacity is achieved at full contraction. However, owing to experimental limitations at 100% contraction—specifically, the load cell's inability to accurately measure the force without deformation—we focused on the 80% contraction level for our optimization. This approach allowed us to obtain reliable data while capturing the performance of the actuator near full contraction.

By analyzing the impact of each design parameter, structures with a higher number of sides (n) tend to maintain greater forces at the same contraction levels than those with fewer sides. Shorter structures (smaller h) exhibit less of a decrease in force as the contraction level increases, indicating better performance under significant contraction. Regarding the origami factor (o), lower values result in a smaller reduction in force as contraction increases, whereas higher values of o lead to a more pronounced decrease in force. This suggests that minimizing the origami factor enhances the force output of the actuator at high contraction levels.

Under no contraction (0% contraction level), the force increases linearly with increasing pressure (Figure 3c). In this state, structures with more sides generate greater forces, and taller structures exhibit higher forces at the same pressure levels. Additionally, a higher origami factor contributes to a greater force under the same pressure conditions without contraction.

Even at significant contraction (80% contraction level), increasing the pressure results in an increase in force (Figure 3d). In this contracted state, structures with more sides continue to produce greater forces, and taller structures maintain higher forces. Interestingly, although a higher origami factor contributes to a greater force when contraction is applied, its impact differs from that of the uncontracted state. This comprehensive analysis underscores the influence of each design parameter on the performance of the actuator under various operating conditions, thereby guiding the optimization of the actuator for maximum payload capacity.

Figure 4a illustrates the force at 70 kPa under 80% strain, represented along the n, h, and o parameters. The first graph shows the variation in force with respect to the number of sides (n) while maintaining the height ($h = 24$) and origami factor ($o = 1$) as constants. It indicates a rapid increase in force as the number of sides increases, saturating when n exceeds 8. The second graph shows the change in force concerning height (h), with the number of sides ($n = 8$) and origami factor ($o = 1$) held constant. It can be observed that the force decreases as height increases. The final graph shows the change in force with respect to the origami factor (o), where the number of sides ($n = 8$) and height ($h = 24$) remain constant. As o decreases from 1 to 0, the force increases significantly.

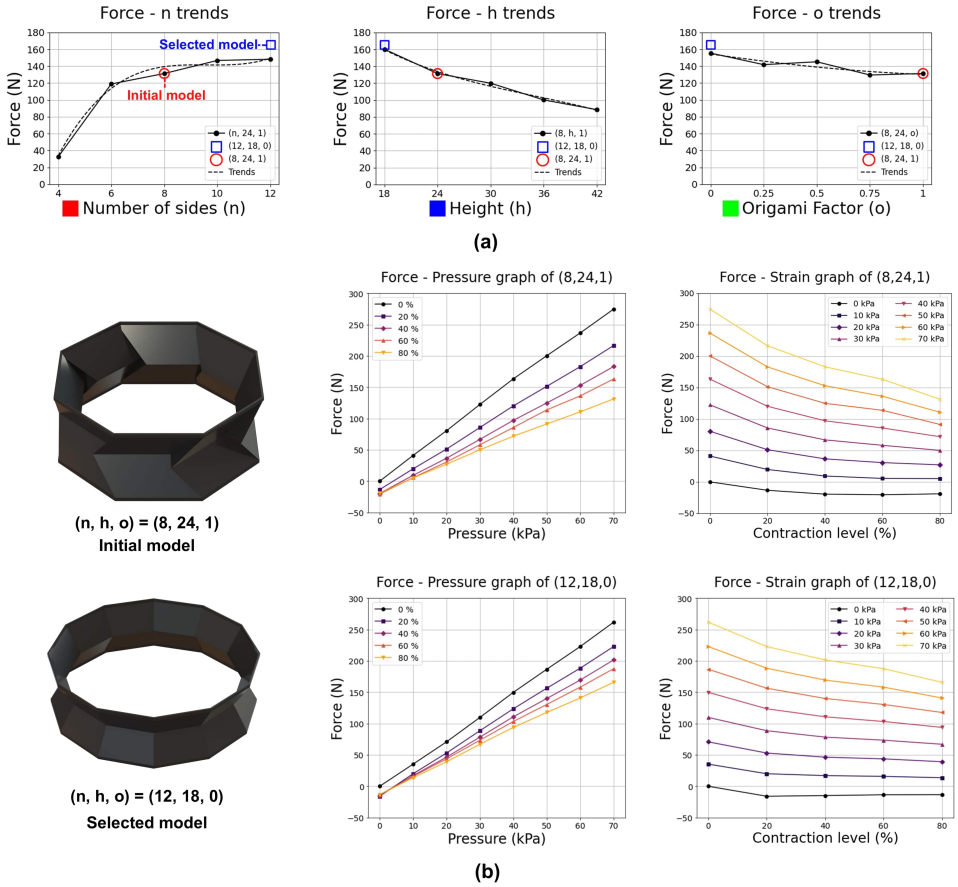


Figure 4. (**a**) Force trends as a function of n, h, and o. (**b**) Comparison of force responses for the initial model $(n, h, o) = (8, 24, 1)$ and optimized model $(n, h, o) = (12, 18, 0)$ under varying pressure and contraction levels.

For each axis—n, h, and o—the values that resulted in the highest force were selected as the optimal model. Based on these tendencies, the combination $(n, h, o) = (12, 18, 0)$ was selected as the optimized model, providing the highest force among the tested configurations. This model exhibits a 21.48% increase in force compared to the initial model.

Figure 4b presents a detailed comparison between the optimized model and the initial model $(n, h, o) = (8, 24, 1)$. The top two graphs in Figure 4b show the relationships between force and pressure and between force and strain for the initial model, whereas the bottom two graphs show the corresponding relationships for the optimized model. Although the selected model produced a lower force than the initial model under all pressures in the unstrained state, it exhibited a higher force at 80% strain across all pressures. This indicates that the selected model has a greater payload capacity.

An actuator based on selected values $(n, h, o) = (12, 18, 0)$ is referred to as a unidirectional bellows pneumatic artificial muscle (UniBPAM). By minimizing the origami factor o, the actuator adopts a bellows-like structure, thereby enhancing its performance under high-strain conditions.

2.3. Scalability

To explore the scalability of the UniBPAM design, the diameter D of the actuator, initially set to 72 mm, was varied. By normalizing the design variables h and p (associated with the origami factor o), the parameters remain dimensionless. This normalization enables the scaling of UniBPAM while preserving the geometric proportions dictated by h and o.

Experiments were conducted using scaled versions of UniBPAM with diameters reduced to $\frac{1}{2}D$ (36 mm) and increased to $2D$ (144 mm) to assess how changes in size affect performance. To maintain consistency, the scaled actuators were fabricated using the same materials and manufacturing processes as the original design. Figure 5 shows the different sizes of UniBPAM prototypes used in these experiments.

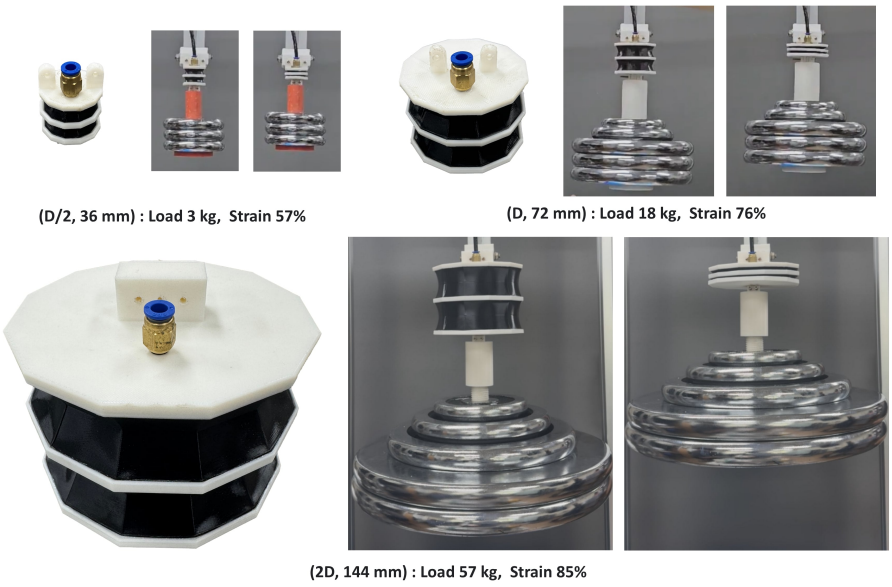


Figure 5. Scaled UniBPAM prototypes with diameters of $\frac{1}{2}D$ (36 mm), D (72 mm), and $2D$ (144 mm).

Payload tests were performed on each scaled UniBPAM to evaluate the force generation and contraction capabilities at an operating pressure of -62 kPa. The experimental setup was identical to that described in the actuator test section, ensuring that any performance differences can be attributed to scaling effects, as opposed to experimental inconsistencies.

The final lengths after contraction were recorded, and the contraction rates for each scaled actuator were calculated, as listed in Table 2. The 36 mm-diameter actuator exhibited a contraction rate of approximately 57%, lifting a payload of 3 kg. The 72 mm-diameter actuator exhibited a contraction rate of approximately 76%, lifting 18 kg, and the 144 mm-diameter actuator achieved a contraction rate of approximately 85%, lifting 57 kg. These results indicate that larger actuators achieve higher contraction rates than smaller actuators and can lift significantly heavier payloads. This is because, as the size increases, $\frac{dV}{dx}$ increases,

resulting in greater force, and the proportion of the rigid constraint in the total length of the actuator decreases, leading to an increase in strain.

Table 2. Performance of scaled UniBPAM actuators at 62 kPa operating pressure.

Diameter (mm)	Initial Length (mm)	Displacement (mm)	Strain (%)	Payload (kg)
36	24.0	13.6	56.7	3
72	42.8	32.5	75.9	18
144	79.5	67.5	84.9	57

Despite the smaller absolute displacements, larger actuators exhibit higher contraction rates and payload capacities. The 144 mm-diameter actuator, with a contraction rate of approximately 85%, was able to lift a payload of 57 kg, whereas the 36 mm-diameter actuator, with a contraction rate of approximately 57%, could lift only 3 kg. This suggests that larger actuators not only generate greater absolute forces, owing to their increased size, but also achieve greater proportional contractions.

These findings confirm the versatility and scalability of the UniBPAM design. By adjusting the actuator size, we can tailor the force output and contraction characteristics to meet specific application requirements, supporting the potential for customizing UniBPAM actuators for a wide range of applications that require different force outputs and sizes.

3. Application to Robotic Joints

3.1. Bidirectional Actuators

By applying a lateral surface pattern with parameters (12, 18, 0), we modified the original BiPAM design to create the Bidirectional Bellows Pneumatic Artificial Muscle (BiBPAM) [19]. The structure of BiBPAM mirrors the foundational design of BiPAM while incorporating these new lateral surface patterns.

Figure 6a shows an expanded view of the BiBPAM layer. The structure comprises an external pattern, an internal pattern, a rigid plate, and a tendon. These components are combined to form a single operational unit, with the external and internal patterns playing a critical role in generating motion by maintaining pneumatic pressure within each chamber. The internal pattern forms chambers that allow the tendon to move internally, whereas the external pattern is printed by stacking layers at one-third of its diameter (D/3) across the three levels. Additionally, the rigid plate, shaped like a wheel, constrains the movement of the external and internal patterns, ensuring that they move cohesively.

We developed two versions based on the selected model: single-chamber bidirectional bellows pneumatic artificial muscles (BiBPAM-S) and dual-chamber bellows bidirectional pneumatic artificial muscles (BiBPAM-D). Figure 6b illustrates the assembly of BiBPAM-S. This module features a single chamber with a multilayer structure, where each layer is interconnected around the central tendon, efficiently transmitting the linear motion generated via both vacuum and pneumatic pressure. This design enables unidirectional linear motion with a single chamber.

Figure 6c shows BiBPAM-D. The dual-chamber structure comprises upper and lower chambers separated by a central middle plate. Each chamber connects to an independent pneumatic supply line, allowing for bidirectional motion. Therefore, the chambers can be controlled independently. Additionally, each chamber can combine forces in the same direction when positive/negative or negative/positive pressure is applied. To prevent the buckling of the external structure, a flexible frame was incorporated.

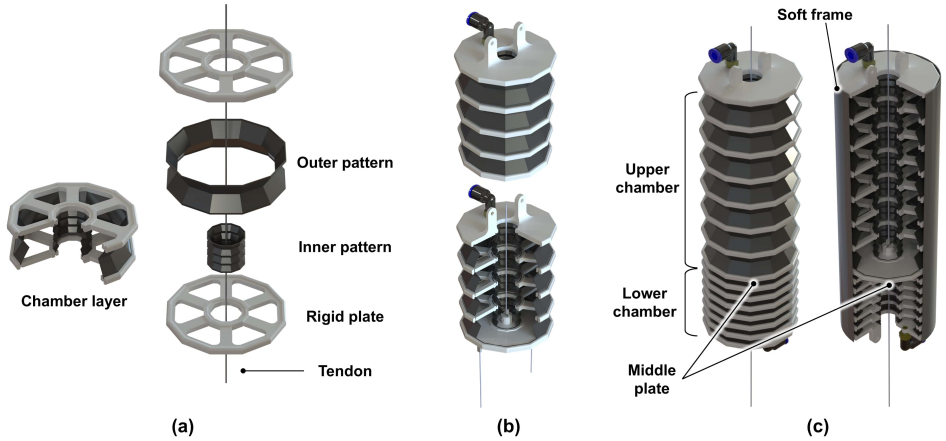


Figure 6. (**a**) Exploded view of the BiBPAM layer, showing the outer and inner patterns, rigid plate, and tendon. (**b**) Assembly of the BiBPAM-S, featuring the stacked chamber layers forming a modular actuator. (**c**) Cross-sectional view of the BiBPAM-D, showing the soft frame and the upper and lower chambers.

3.2. Control System

We proposed pneumatic circuits for BiBPAM-S and BiBPAM-D, as shown in Figure 7a. Positive pressure is generated via a compressor (OS-300, ACOM, Uiwang-si, Republic of Korea), and a portion of this pressure is used to produce negative pressure (vacuum) through a vacuum generator (SCPSi-L-3-20 HV, SCHMALZ, Glatten, Germany). In this system, the vacuum and positive pressure pass through a vacuum regulator (ITV-2090, SMC, Tokyo, Japan) and positive pressure regulator (ITV-2030, SMC, Tokyo, Japan), respectively, and their flow rates are controlled via proportional control valves (MPYE-5-1/8-HF, FESTO, Esslingen, Germany). The regulated flows are then supplied to the actuator through a five-port, three-position valve (VUVG-L10-P53C, FESTO, Esslingen, Germany).

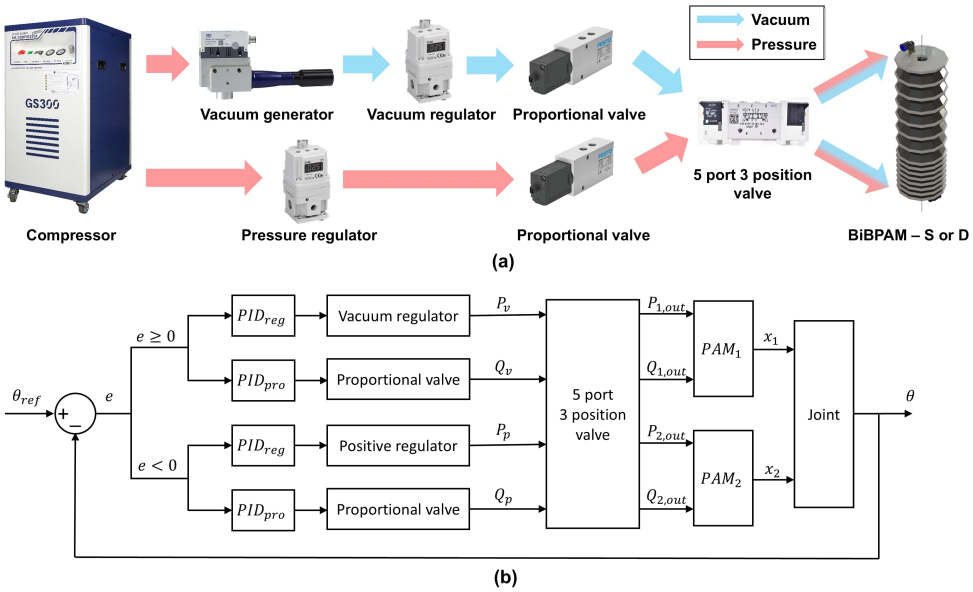


Figure 7. (**a**) Configuration of the pneumatic control system for the BiBPAMs. (**b**) Control flow diagram illustrating the use of PID controllers for system regulation.

Furthermore, to control the configured pneumatic circuit, we constructed a control system, as shown in Figure 7b. The main objective of this system is to minimize the error, defined as the difference between the reference value, θ_{ref}, and the actual value, θ. The error

value, e, is expressed as $e = \theta_{\text{ref}} - \theta$. This error value is processed through a PID controller described by the following equation:

$$\text{PID}_X = K_P\left(e + \frac{1}{T_i}\int e\,dt + T_d\frac{de}{dt}\right) \tag{6}$$

where K_P denotes the proportional gain, T_i denotes the integral time constant, and T_d denotes a derivative time constant. Additionally, X represents either *reg* or *pro*, depending on the control target.

Depending on the sign of the error value, e, the system connects different pressure sources to BiBPAM-S and BiBPAM-D. When the error value is greater than or equal to zero ($e \geq 0$), the five-port, three-position valve selects the negative pressure (P_V) generated via the vacuum generator and directs it to BiBPAM-D. Conversely, if the error value is less than zero ($e < 0$), then the positive pressure (P_P) generated via the positive pressure regulator is delivered to the BiBPAM-D. In this process, the five-port, three-position valve operates as follows:

$$\begin{aligned}
\text{if } e \geq 0: \quad & P_{1,\text{out}} = P_V, \quad Q_{1,\text{out}} = Q_V \\
& P_{2,\text{out}} = P_P, \quad Q_{2,\text{out}} = Q_P \\
\text{if } e < 0: \quad & P_{1,\text{out}} = P_P, \quad Q_{1,\text{out}} = Q_P \\
& P_{2,\text{out}} = P_V, \quad Q_{2,\text{out}} = Q_V
\end{aligned}$$

This switching mechanism supplies the appropriate pressure to both BiBPAM-S and BiBPAM-D, allowing the system to be controlled to match the reference value. When air is delivered to the actuators, a displacement occurs due to actuator movement, and this displacement is transmitted to the joint through the tendon, causing joint rotation and resulting in a change in angle θ.

The difference between BiBPAM-S and BiBPAM-D is that BiBPAM-D has a dual-chamber structure, where positive and negative pressures can be independently connected to each chamber. In contrast, BiBPAM-S operates as a single-chamber system, with the second chamber vented to atmospheric pressure through $P_{2,\text{out}}$ and $Q_{2,\text{out}}$. Therefore, in BiBPAM-S, only the pressure in the first chamber affects the joint rotation, whereas, in BiBPAM-D, the pressures in both chambers contribute to the rotational movement, allowing for more precise control.

3.3. Forearm

The forearm mechanism was designed using a BiBPAM-S actuator, rotary encoder, and wrist pulley, along with Tendons #1, #2, and #3. The pulley consists of three layers: Tendon #1 and Tendon #3 are located in the first and third layers, while Tendon #2 is positioned in the second layer. The actuator is connected to the wrist pulley via tendons. When the actuator depressurizes and contracts, tension is applied to Tendon #1 and Tendon #3, inducing clockwise rotation. Conversely, when it pressurizes and expands, tension is applied to Tendon #2, causing the pulley to rotate counterclockwise. The rotation angle is precisely measured via a rotary encoder (Figure 8a).

Experiments were conducted by connecting the pneumatic system and actuator with PID control to evaluate performance via a step response. A ball with two alternating colors, representing different angles, was attached to the forearm for an easy visualization of the angle changes (Figure 8b).

The forearm mechanism demonstrates a sequence of rotations from 0 to 160 degrees in 20-degree increments. The frequency-response characteristics were tested from 0.2 Hz to 1 Hz at intervals of 0.2 Hz, with an additional test at 2 Hz. At frequencies exceeding 0.6 Hz, the control system could not follow the target angles. The −3 dB line in the graph represents the bandwidth, which indicates the performance limitations of the control system (Figure 8c,d).

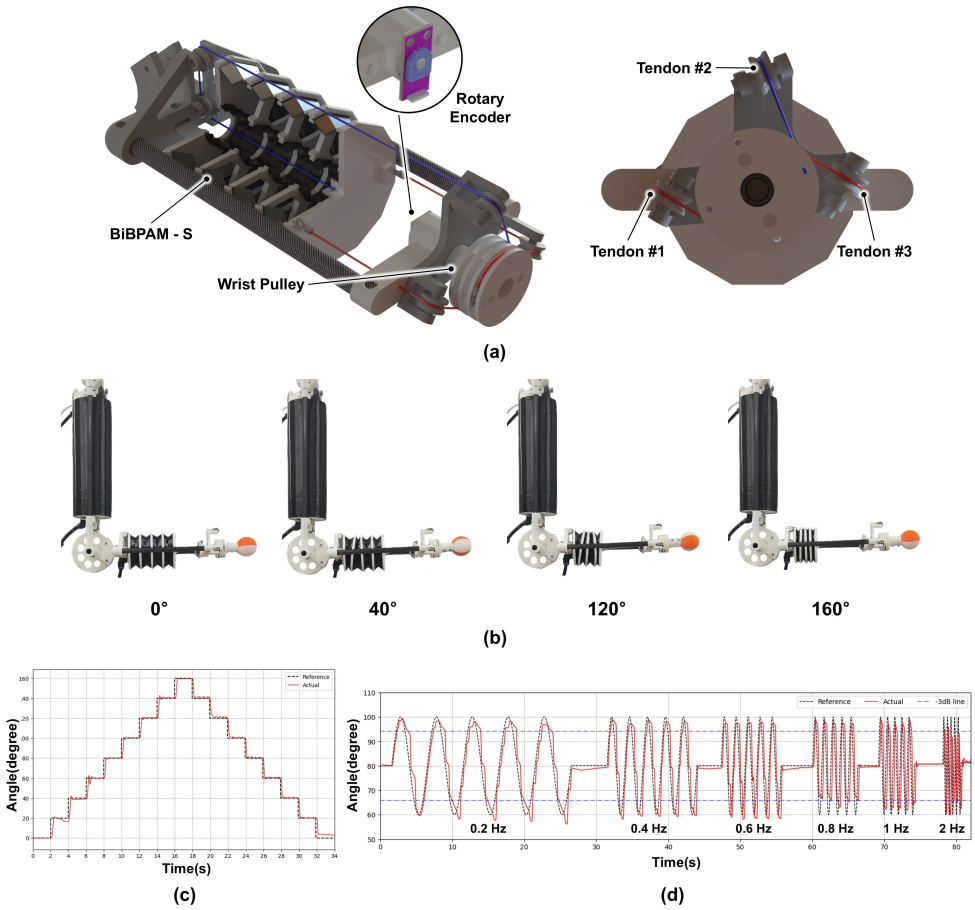


Figure 8. (**a**) Diagram of the forearm mechanism, highlighting the BiBPAM-S actuator, rotary encoder, wrist pulley, and tendon pathways for expansion and contraction. (**b**) Sequential images depicting the robotic arm's movement at different angles (0°, 40°, 80°, and 160°). (**c**) Time response showing the wrist angular position as a function of time. (**d**) Frequency response illustrating the system's frequency response, with a marked −3 dB line indicating the bandwidth.

The regulator gain values of the control system were tuned and set to $K_p = 0.1$ and $T_i = 0.001$, whereas the gain values of the proportional control valve were tuned to $K_p = 0.12$, $T_i = 0.05$ and $T_d = 0.001$.

3.4. Upper Arm

The upper-arm mechanism was designed using a BiBPAM-D actuator, a rotary encoder, an upper tendon, a lower tendon, and an elbow pulley. Based on the middle plate of the BiBPAM-D, the upper tendon is located above, and the lower tendon is located below. These two tendons meet at the circumference of the elbow pulley (Figure 9a). The actuator connects to the upper arm pulley through tendons, enabling controlled movement of the upper arm. The rotary encoder measures the rotation angle of the pulley, providing precise feedback to the control system.

Experiments were conducted by connecting the pneumatic system to the actuator, with PID control implemented to evaluate performance through a step response. To visualize the changes in angle during operation, four different positions were marked on the upper arm (Figure 9b).

The frequency response test was conducted from 0.2 Hz to 1 Hz at 0.2 Hz intervals, with additional tests at 2 Hz and 3 Hz. At frequencies exceeding 0.6 Hz, the control system exhibited difficulty in tracking the target angles. The −3 dB line in the graph indicates the bandwidth, indicating the performance limits of the system (Figure 9c,d). For the control

system, the regulator gain values were tuned and set to $K_p = 0.05$ and $T_i = 0.05$, whereas the gain values of the proportional control valve were set to $K_p = 0.1$ and $T_d = 0.001$.

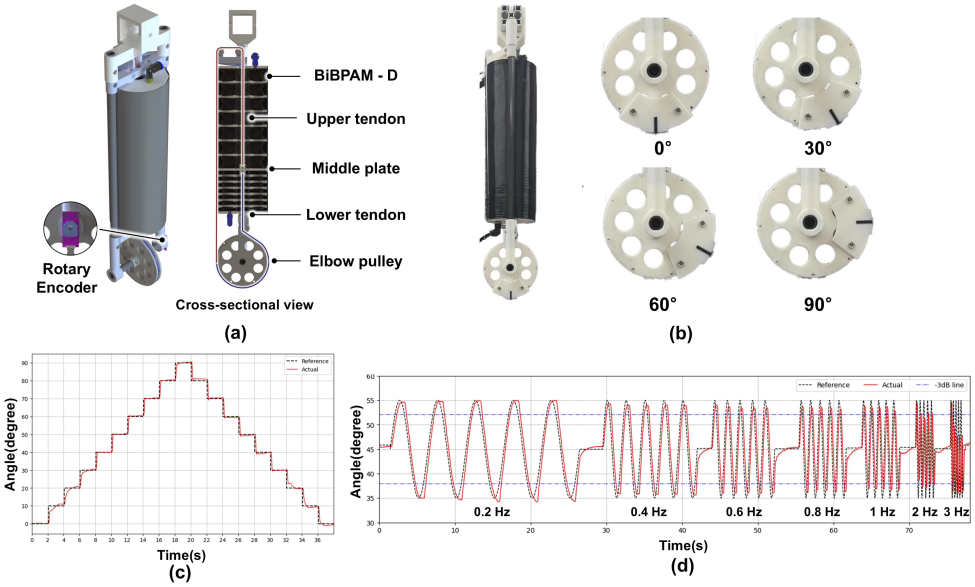


Figure 9. (**a**) Diagram of the robotic arm's mechanism highlighting the BiPAM-D actuator, rotary encoder, upper tendon, lower tendon, and elbow pulley. (**b**) Sequential images depicting the upper arm's movement at different angles (0°, 30°, 60°, and 90°). (**c**) Time response illustrating the upper arm's angular position over time. (**d**) Frequency response displaying the upper arm system's frequency response with a -3 dB line denoting the bandwidth.

4. Conclusions

In this study, we introduced a novel soft pneumatic actuator that builds upon the capabilities of existing actuators in soft robotics. While previous designs often did not fully achieve a balanced combination of high force generation, large strain capability, bidirectional actuation, ease of fabrication, and scalability, our actuator utilizes 3D printing technology to integrate all of these characteristics simultaneously.

We commenced by analyzing key design parameters—such as the number of sides (n), height (h), and origami factor (o)—to optimize the performance of the actuator. Through experimental validation, we identified the optimal configuration, $(n, h, o) = (12, 18, 0)$, which we termed UniBPAM. This optimized design achieved a 21.48% increase in force at an 80% contraction level compared to the initial model, demonstrating enhanced performance under high-strain conditions.

Furthermore, we explored the scalability of UniBPAM by fabricating and testing actuators with diameters ranging from 36 mm to 144 mm. The results confirmed that larger actuators not only generated greater absolute forces but also achieved higher proportional contractions, validating the design's scalability and versatility for various applications. Specifically, the scaled actuators were capable of lifting payloads up to 57 kg. For instance, the 144 mm-diameter actuator achieved 84.9% strain while lifting a 57 kg load, demonstrating the actuator's significant load-bearing capacity at larger scales.

Building on UniBPAM, we developed BiBPAM in BiBPAM-S and BiBPAM-D configurations. These actuators were applied to robotic joints, specifically in the forearm and upper arm mechanisms, enabling bidirectional torque generation and controlled joint movements. The control system, implemented using PID controllers, successfully managed the pneumatic circuits to achieve precise positioning. Performance evaluations through position-control and frequency-response experiments demonstrated acceptable response times and bandwidths suitable for robotic applications.

The proposed actuator demonstrated significant improvements in force generation and scalability, and future research will explore methods for single-step printing without

adhesive to simplify the fabrication process. Although bidirectional operation is now possible, improving the actuator's control precision would also be beneficial for broader robotic applications.

Author Contributions: Conceptualization, J.H.P.; methodology, S.J., Y.J.G., J.Y. and B.G.K.; software, D.S.; validation, J.H.P., J.Y. and H.-W.S.; formal analysis, Y.J.G. and J.Y.; investigation, D.S. and H.-W.S.; resources, H.R.C.; data curation, J.H.P. and B.G.K.; writing—original draft preparation, J.H.P.; writing—review and editing, J.H.P.; visualization, S.J. and Y.J.G.; supervision, R.H. and H.R.C.; project administration, J.C.K., H.M., R.H. and H.R.C. All authors have read and agreed to the published version of the manuscript.

Funding: This work was supported by the National Research Foundation of Korea (NRF) grant funded by the Korea government (MSIT) (RS-2023-00207772) and by the Ministry of Trade, Industry and Energy (Project No. 1415187105).

Institutional Review Board Statement: Not applicable.

Informed Consent Statement: Not applicable.

Data Availability Statement: Data are contained within the article.

Conflicts of Interest: The authors declare no conflicts of interest.

Abbreviations

The following abbreviations are used in this manuscript:

PAM	Pneumatic artificial muscle
3D	Three-dimensional
UniBPAM	Unidirectional Bellows Pneumatic Artificial Muscles
BiBPAM	Bidirectional Bellows Pneumatic Artificial Muscles
BiBPAM-S	Single-Chamber Bidirectional Bellows Pneumatic Artificial Muscles
BiBPAM-D	Dual-Chamber Bidirectional Bellows Pneumatic Artificial Muscles
PID	Proportional–integral–derivative

References

1. Ilievski, F.; Mazzeo, A.D.; Shepherd, R.F.; Chen, X.; Whitesides, G.M. Soft robotics for chemists. *Angew. Chem. Int. Ed.* **2011**, *50*, 1890–1895. [CrossRef] [PubMed]
2. Polygerinos, P.; Correll, N.; Morin, S.A.; Mosadegh, B.; Onal, C.D.; Petersen, K.; Cianchetti, M.; Tolley, M.T.; Shepherd, R.F. Soft robotics: Review of fluid-driven intrinsically soft devices; manufacturing, sensing, control, and applications in human-robot interaction. *Adv. Eng. Mater.* **2017**, *19*, 1700016. [CrossRef]
3. Joe, S.; Bernabei, F.; Beccai, L. A Review on Vacuum-Powered Fluidic Actuators in Soft Robotics. In *Rehabilitation of the Human Bone-Muscle System*; Olaru, A., Ed.; IntechOpen: Rijeka, Croatia, 2022; Chapter 5.
4. Chou, C.P.; Hannaford, B. Measurement and modeling of McKibben pneumatic artificial muscles. *IEEE Trans. Robot. Autom.* **1996**, *12*, 90–102. [CrossRef]
5. Tondu, B.; Lopez, P. Modeling and control of McKibben artificial muscle robot actuators. *IEEE Control Syst. Mag.* **2000**, *20*, 15–38.
6. Klute, G.K.; Czerniecki, J.M.; Hannaford, B. McKibben artificial muscles: Pneumatic actuators with biomechanical intelligence. In Proceedings of the 1999 IEEE/ASME International Conference on Advanced Intelligent Mechatronics (Cat. No. 99TH8399), Atlanta, GA, USA, 19–23 September 1999; pp. 221–226.
7. Hawkes, E.W.; Blumenschein, L.H.; Greer, J.D.; Okamura, A.M. A soft robot that navigates its environment through growth. *Sci. Robot.* **2017**, *2*, eaan3028. [CrossRef] [PubMed]
8. Putzu, F.; Abrar, T.; Althoefer, K. Plant-inspired soft pneumatic eversion robot. In Proceedings of the 2018 7th IEEE International Conference on Biomedical Robotics and Biomechatronics (Biorob), Enschede, The Netherlands, 26–29 August 2018; pp. 1327–1332.
9. Hawkes, E.W.; Christensen, D.L.; Okamura, A.M. Design and implementation of a 300% strain soft artificial muscle. In Proceedings of the 2016 IEEE International Conference on Robotics and Automation (ICRA), Stockholm, Sweden, 16–21 May 2016; pp. 4022–4029.
10. Li, S.; Vogt, D.M.; Rus, D.; Wood, R.J. Fluid-driven origami-inspired artificial muscles. *Proc. Natl. Acad. Sci. USA* **2017**, *114*, 13132–13137. [CrossRef] [PubMed]
11. Oguntosin, V.; Akindele, A. Design and characterization of artificial muscles from wedge-like pneumatic soft modules. *Sens. Actuators A Phys.* **2019**, *297*, 111523. [CrossRef]
12. Felt, W.; Robertson, M.A.; Paik, J. Modeling vacuum bellows soft pneumatic actuators with optimal mechanical performance. In Proceedings of the 2018 IEEE International Conference on Soft Robotics (RoboSoft), Livorno, Italy, 24–28 April 2018; pp. 534–540.

13. Kulasekera, A.L.; Arumathanthri, R.B.; Chathuranga, D.S.; Gopura, R.; Lalitharatne, T.D. A thin-walled vacuum actuator (ThinVAc) and the development of multi-filament actuators for soft robotic applications. *Sens. Actuators A Phys.* **2021**, *332*, 113088. [CrossRef]
14. Lee, J.G.; Rodrigue, H. Origami-based vacuum pneumatic artificial muscles with large contraction ratios. *Soft Robot.* **2019**, *6*, 109–117. [CrossRef] [PubMed]
15. Li, S.; Vogt, D.M.; Bartlett, N.W.; Rus, D.; Wood, R.J. Tension pistons: Amplifying piston force using fluid-induced tension in flexible materials. *Adv. Funct. Mater.* **2019**, *29*, 1901419. [CrossRef]
16. Coutinho, A.; Park, J.H.; Jamil, B.; Choi, H.R.; Rodrigue, H. Hyperbaric Vacuum-Based Artificial Muscles for High-Performance Actuation. *Adv. Intell. Syst.* **2023**, *5*, 2200090. [CrossRef]
17. Usevitch, N.S.; Okamura, A.M.; Hawkes, E.W. APAM: Antagonistic pneumatic artificial muscle. In Proceedings of the 2018 IEEE International Conference on Robotics and Automation (ICRA), Brisbane, Australia, 21–25 May 2018; pp. 1539–1546.
18. Chen, Y.; Zhang, J.; Gong, Y. Novel Design and Modeling of a Soft Pneumatic Actuator Based on Antagonism Mechanism. *Actuators* **2020**, *9*, 107. [CrossRef]
19. Park, J.H.; Kim, K.; Gong, Y.J.; Yang, S.Y.; Hwang, S.T.; Jung, H.S.; Moon, H.; Koo, J.C.; Rodrigue, H.; Choi, H.R. Cooperative antagonistic mechanism driven by bidirectional pneumatic artificial muscles for soft robotic joints. *Mechatronics* **2024**, *97*, 103099. [CrossRef]
20. Yap, H.K.; Ng, H.Y.; Yeow, C.H. High-force soft printable pneumatics for soft robotic applications. *Soft Robot.* **2016**, *3*, 144–158. [CrossRef]
21. MacCurdy, R.; Katzschmann, R.; Kim, Y.; Rus, D. Printable hydraulics: A method for fabricating robots by 3D co-printing solids and liquids. In Proceedings of the 2016 IEEE International Conference on Robotics and Automation (ICRA), Stockholm, Sweden, 16–21 May 2016; pp. 3878–3885.
22. Drotman, D.; Ishida, M.; Jadhav, S.; Tolley, M.T. Application-driven design of soft, 3-D printed, pneumatic actuators with bellows. *IEEE/ASME Trans. Mechatronics* **2018**, *24*, 78–87. [CrossRef]
23. Tawk, C.; Spinks, G.M.; in het Panhuis, M.; Alici, G. 3D printable linear soft vacuum actuators: Their modeling, performance quantification and application in soft robotic systems. *IEEE/ASME Trans. Mechatronics* **2019**, *24*, 2118–2129. [CrossRef]
24. Zhang, Z.; Fan, W.; Chen, G.; Luo, J.; Lu, Q.; Wang, H. A 3D printable origami vacuum pneumatic artificial muscle with fast and powerful motion. In Proceedings of the 2021 IEEE 4th International Conference on Soft Robotics (RoboSoft), New Haven, CT, USA, 12–16 April 2021; pp. 551–554.
25. Fan, W.; Wang, J.; Zhang, Z.; Chen, G.; Wang, H. Vacuum-driven parallel continuum robots with self-sensing origami linkages. *IEEE/ASME Trans. Mechatronics* **2024**, *29*, 3370–3380. [CrossRef]
26. Xu, Q.; Zhang, K.; Ying, C.; Xie, H.; Chen, J.; E, S. Origami-Inspired Vacuum-Actuated Foldable Actuator Enabled Biomimetic Worm-like Soft Crawling Robot. *Biomimetics* **2024**, *9*, 541. [CrossRef] [PubMed]
27. Yang, Y.p.; Tian, H.l.; Jiao, S.j. Product design evaluation method using consensus measurement, network analysis, and AHP. *Math. Probl. Eng.* **2019**, *2019*, 4042024. [CrossRef]
28. Villanueva, P.; Bona, S.; Lostado-Lorza, R.; Veiga, F. Morphological design of a bicycle propulsion component using the hierarchical analysis process (AHP). *Appl. Sci.* **2023**, *13*, 7792. [CrossRef]

Disclaimer/Publisher's Note: The statements, opinions and data contained in all publications are solely those of the individual author(s) and contributor(s) and not of MDPI and/or the editor(s). MDPI and/or the editor(s) disclaim responsibility for any injury to people or property resulting from any ideas, methods, instructions or products referred to in the content.